Nanoscale

COMMUNICATION

View Article Online
View Journal | View Issue

Cite this: *Nanoscale*, 2025, **17**, 27200

Received 25th July 2025,
Accepted 29th September 2025

DOI: 10.1039/d5nr03147h

rsc.li/nanoscale

Two dimensional-material-coated microcantilevers for enhanced mass sensing and material characterization

Gourav Bhattacharya, †[a] Indrianita Lionadi,†[a] Stuart McMichael,[a] Mike P. C. Taverne,[b,c] James McLaughlin,[a] Pilar Fernandez-Ibanez,[a] Chung-Che Huang,*[d] Ying-Lung Daniel Ho*[b,c] and Amir Farokh Payam *[a]

The integration of 2D material coatings on microcantilevers marks a transformative advancement in nanomechanical sensing. As essential components of nanomechanical sensors, microcantilevers detect minute forces, such as molecular interactions, through frequency shift measurements, enabling ultra-sensitive detection with atomic-scale mass resolution. This work emphasizes the novelty of employing 2D-material coatings on microcantilevers, presenting an integrated approach that combines theoretical modeling, simulation, and experimentation. By utilizing 2D-material-coated microcantilevers, this study demonstrates the precise measurement of mass, Young's modulus and thickness of 2D material layers. The enhanced performance of these coated resonators is showcased in applications such as bacterial and uric acid mass sensing at varying concentrations, achieving superior frequency detection, responsivity, and accuracy. This research not only advances nanoscale sensor design but also underscores the potential of 2D-material coatings in revolutionizing nanoelectromechanical sensors for materials characterization and mass spectrometry, paving the way for next-generation sensing technologies.

Introduction

Microcantilevers play a central role in imaging and sensing in both atomic force microscopy (AFM) and nanoelectromechanical sensors.[1–6] Thanks to the progress in micro- and nanofabrication technologies, we can now create smaller cantilever-based nanomechanical resonators. These miniature structures are adept at detecting forces, masses, mechanical properties, and motion associated with molecular interactions and surface forces at the molecular/atomic levels.[7–11]

For mass measurements, nanomechanical devices have undergone significant advancements, reaching a stage where they present a compelling opportunity to revolutionize mass spectrometry. Nanoelectromechanical system (NEMS) resonators exhibit remarkable sensitivity, or, in other words, responsivity to the added mass of adsorbed particles.[12–16] This progress has resulted in significant achievements, including the detection of the mass of individual proteins,[17] nanoparticles,[18,19] and large biomolecules.[20,21] Moreover, there have been demonstrations of near-atomic-scale mass resolution.[22,23]

However, when the mass and size of the adsorbent significantly differ from the mass and geometry of the cantilever, accurate mass quantification is compromised. This is due to the microcantilever's sensitivity and the coupling between changes in its stiffness and mass. As a result, this could lead to mismatches in the detected masses potentially exceeding 50%.[9] Another finding of the research indicates that when microcantilevers are used in applications with adsorbed layers, the mechanical properties of these coated cantilevers can show substantial variations compared to their pristine counterparts.[7,19] Previous studies have elucidated that variations in the spring constant of microcantilevers are attributed to alterations in stress on one side of the cantilever.[7] Nevertheless, in those experiments, the effect of the mass of the adsorbed layer was negligible due to the cantilever being considerably larger in mass compared to the adsorbed layer. While some studies have attempted to address the influence of the particle mass and spatial distribution on nanoscale sensors,[24] the phenomenon of observed anomalous frequency shifts requires further investigation.[25] Furthermore, despite significant advancements in using microcantilevers as sensing tools, their characterization capability remains elusive.

Recent advances in the synthesis and preparation of 2D materials[26,27] provide a significant opportunity to utilize them

[a]*Nanotechnology and Integrated Bioengineering Centre, School of Engineering, Ulster University, Belfast, UK. E-mail: a.farokh-payam@ulster.ac.uk*
[b]*Department of Mathematics, Physics & Electrical Engineering, Northumbria University, NE1 8ST Newcastle upon Tyne, UK. E-mail: daniel.ho@northumbria.ac.uk*
[c]*Department of Electrical and Electronic Engineering, University of Bristol, BS8 1UB Bristol, UK*
[d]*Electronics & Computer Science, University of Southampton, SO17 1BJ, Southampton, UK. E-mail: cch@soton.ac.uk*
†These authors contributed equally to this work.

in microcantilever-based nanomechanical sensors and energy harvesters.[28] These novel materials can be applied as a coating to microcantilevers, enhancing their ability to detect with high responsivity. For example, molybdenum disulfide (MoS_2) has unique physical and mechanical properties, such as high surface area, flexibility and stiffness,[29] which can be adjusted by changing the number of layers or incorporating defects. This tunability allows for the customization of cantilever designs with desired mechanical characteristics for specific sensing applications. The surface of MoS_2 can be easily functionalized[28] and it also possesses tunable higher electron mobility.[28] These properties make it a suitable candidate for an efficient sensing platform. This integration of 2D materials with microcantilevers allows for precise control over the cantilever's resonant frequency and significant improvements in the minimum detectable frequency and sensitivity of mass spectrometry, enabling applications in high-precision sensing.

In this work, we employ the concept of a digital twin to develop an integrated theoretical, simulation and experimental methodology. This method elucidates the effect of coating and layer adsorption mechanisms on the characteristics of nanomechanical resonators, explores the origin of observed anomalous frequency shifts, and quantifies the properties of the coated layers.

Experimentally, we introduce a technique to uniformly coat the microcantilever surface with large-scale MoS_2 through van der Waals epitaxy. Subsequently, the theoretical model allows us to measure the mass and quantify Young's modulus, thickness, and layer count of MoS_2 directly from the measured frequency and spring constant of the coated microcantilever. We used two methods to determine the mass, thickness, and Young's modulus of the deposited MoS_2. In Method 1, Raman spectroscopy and high resolution transmission electron microscopy (HRTEM) were employed to determine the number of MoS_2 layers. Using the cantilever's geometry, we calculated the MoS_2 mass, which, combined with frequency measurements, allowed us to compute the cantilever's spring constant. Applying composite beam theory, we then extracted the Young's modulus of the MoS_2 layer. In Method 2, we measured the cantilever's frequency and spring constant before and after MoS_2 deposition. Using an updated cantilever mass spectrometry model, we calculated the MoS_2 mass, and from the mass, frequency shift, and spring constant, we derived its thickness and Young's modulus. We then utilize the MoS_2-coated microcantilever to measure the mass of *Escherichia coli* (*E. coli*) bacteria, demonstrating a significant improvement in its minimum frequency detection, which is approximately 4 times better than that of a pristine cantilever. This results in higher sensitivity and accuracy in mass spectrometry. Furthermore, to show the trends in accurately measuring the mass of adsorbent using the modified MoS_2 microcantilever and also the importance of considering the stiffness change in mass measurements, we used our modified microcantilevers to measure the mass of adsorbed uric acid with different concentrations on the surface of the microcantilevers. Our results clearly show the higher responsivity and accuracy of our modified MoS_2 microcantilever in detecting the mass of added uric acid with different concentrations.

This approach is a breakthrough in the characterization of 2D materials. It could also pave the way for the design and fabrication of a new generation of microcantilevers that benefit from the unique properties of 2D materials for use in sensing applications.

Methodology

The schematic of our integrated methodology is given in Fig. 1. For our presented analysis, the cantilever geometry is approximated as an ideal rectangular shape with coated MoS_2 as a 2D material.

The cantilever is singly clamped at one end and free at the other end. The length of the cantilever is L_c, width b_c and thickness h_c oriented with the x-axis, with flexural displacement along the z-axis. The coated MoS_2 has the same length and width as the cantilever, and its thickness is h_a.

By neglecting rotary inertia and shear deformation, using Galerkin discretization[30] and equalizing the mean values of the cantilever flexural work and kinetic energy per oscillation cycle, the resonance frequencies of the cantilever can be obtained as (see S1 in the Supplementary Information (SI))

$$\omega_n = \sqrt{\frac{\int_0^L \mathrm{EI}_{\mathrm{eq}} \ddot{\varphi}_n{}^2 \mathrm{d}x}{\int_0^L (\rho_c h_c + \rho_a h_a)\varphi_n{}^2 \mathrm{d}x}} \tag{1}$$

where $\varphi_n(x)$ is the nth eigenmode shape of the cantilever to satisfy the boundary conditions,[31] ω_n is the nth eigenfrequency of the cantilever, and ρ_c and ρ_a are the densities of the pristine cantilever and added layer, respectively. $\mathrm{EI}_{\mathrm{eq}}$ is described as[32–34]

$$\begin{aligned}\mathrm{EI}_{\mathrm{eq}} = {} & \frac{E_c h_c{}^3}{3} + \frac{E_a h_a{}^3}{3} + E_c h h_c (h - h_c) \\ & + E_a h_c h_a (h_c + h_a - 2h) + E_a h h_a (h - h_a)\end{aligned} \tag{2}$$

where E_c and E_a are Young's moduli of the cantilever and added layer, respectively, and h is the position of the neutral axis because of the added top layer thickness:

$$h = \frac{E_c h_c{}^2 + E_a (h_a{}^2 + 2h_a h_c)}{2(E_a h_a + E_c h_c)} \tag{3}$$

From eqn (1), we can derive expressions for the critical Young's modulus or critical density of the added layer that will increase the resonant frequency (see S1):

$$\mathrm{EI}_{\mathrm{eq}} > \frac{E_c h_c{}^2 \left(h_c + h_a \frac{\rho_a}{\rho_c}\right)}{12} \tag{4a}$$

and

$$\rho_a < \frac{12 \rho_c \mathrm{EI}_{\mathrm{eq}}}{E_c h_c{}^2 h_a} - \rho_c \frac{h_c}{h_a} \tag{4b}$$

Furthermore, we consider the tip mass effect on our analysis of the cantilever dynamics.

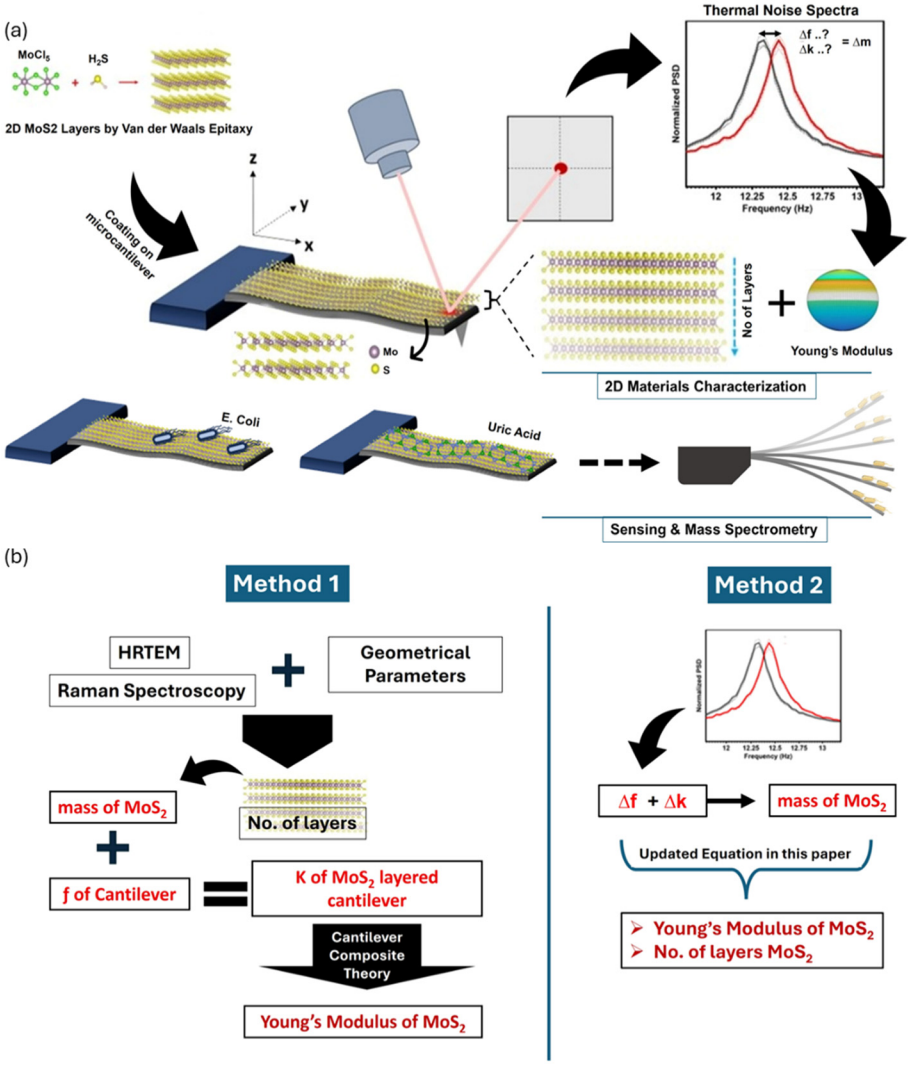

Fig. 1 (a) The schematic of the MoS_2 coating approach and methodology for sensing and characterization. In this work, we utilized the van der Waals epitaxy method to synthesize 2D material layers (*e.g.* MoS_2) and then transferred them over microcantilevers. The thermal noise spectra before and after deposition were recorded to measure the frequency shift and spring constant of microcantilevers before and after deposition. Here, we deconvoluted the mass and stiffness using an analytical model to measure the mass, layer thickness, and the number of layers of the added MoS_2 layer and its Young's modulus. The coated cantilever was finally used as a sensor to measure the mass of *E. coli* bacteria and uric acid concentration in PBS buffer. (b) The schematic of the two methods used for characterization of coated MoS_2. In the first approach, the layers of coated MoS_2 are measured by Raman spectroscopy and/or HRTEM, and then, using cantilever geometry, the mass of MoS_2 is calculated. Subsequently, employing the measured mass and frequency of the coated microcantilever, the spring constant is calculated and used to compute the Young's modulus of MoS_2. In the second approach, by measuring the spring constant and mass of the microcantilever before and after deposition, the mass of MoS_2 is measured and the measured frequency and spring constant are then used to measure the Young's modulus of MoS_2. Created with VESTA, data *via* Materials Project (Creative Commons CC BY 4.0 licence).

Considering the tip mass in the Euler–Bernoulli equation,[35] the characteristic equation is obtained as

$$C(\kappa) = \kappa^3(1+\cos(\kappa)\cosh(\kappa)) + \frac{m_{\mathrm{tip}}\kappa^4}{(\rho_c h_c + \rho_a h_a) b_c L_c}(\sinh(\kappa)\cos(\kappa) - \sin(\kappa)\cosh(\kappa)) \quad (5)$$

where m_{tip} is the tip mass. Then, the frequency of the cantilever is given by

$$f_n = \frac{\kappa^2}{2\pi {L_c}^2}\sqrt{\frac{\mathrm{EI}_{\mathrm{eq}}}{(\rho_c h_c + \rho_a h_a)}} \quad (6)$$

Results and discussion

Initially, to investigate the effect of tip mass on the frequency response of the cantilever, we assumed that the tip mass is between 0 and 15% of the cantilever mass and performed numerical simulations. The results of the first to fourth eigen-

frequencies are given in Fig. 2. As can be seen, for the case that the tip mass is less than 10% of the cantilever mass, which is the case of commercial cantilevers, the tip mass effect is negligible. As Fig. 2 shows, while increasing the thickness of deposition (here, MoS_2) significantly increases the frequency of the cantilever, increasing the mass of the tip has a negligible effect (less than 1%) on the frequency response of the cantilever for all eigenfrequencies, which means that we can neglect its effect on our analysis of the cantilever dynamics.

Then, our combined model is employed to analyze how the thickness and properties of coated materials impact the frequency response of a microcantilever. We conducted calculations to determine the variations in the natural frequency of the modified cantilever as materials with different Young's moduli and densities were deposited on the pristine cantilever. In this study, we focused on two silicon-based microcantilevers, namely SCM-PIC and FMV-A. Although the material properties of both cantilevers are identical, their geometries (length, width, and height) differ. The calculations were performed across a range of added material thicknesses, and the results are illustrated in Fig. 3a and b.

In our observations, we identified a specific density and Young's modulus combination where the polarity of the frequency shift is reversed. We designated this particular frequency as the critical frequency and the corresponding density and Young's modulus values as critical density and critical Young's modulus, respectively. Additionally, our findings indicate that increasing the thickness of added materials results in a positive frequency shift. The magnitude of this frequency shift is more pronounced in the FMV-A cantilever compared to SCM-PIC, reflecting the higher sensitivity of the FMV-A microcantilever. This responsivity can be attributed to the fact that the critical frequency, critical density, and critical Young's modulus are significantly influenced by the type of pristine cantilever and its geometry.

In order to visualise these in a better and simpler way, we have plotted 2D contour plots for 2 different cantilevers, SCM-PIC and FMV-A, and presented them in Fig. S1 (section S2).

In the preceding section, our aim was to investigate how the original cantilever's geometry influences frequency shifts. To expand our analysis and explore the influence of material properties of the pristine cantilever on frequency shifts resulting from layer deposition, we utilized a silicon nitride-based QUEST R 200 cantilever. We then plotted the changes in the natural frequency of the modified cantilever as materials with varying Young's moduli and densities were deposited onto the pristine cantilever at different thickness levels (Fig. S2). The observed variation was similar to that of the silicon-based cantilevers, but the magnitudes of frequency shifts were higher compared to the silicon-based ones, indicating the higher responsivity of the QUEST R 200 cantilever.

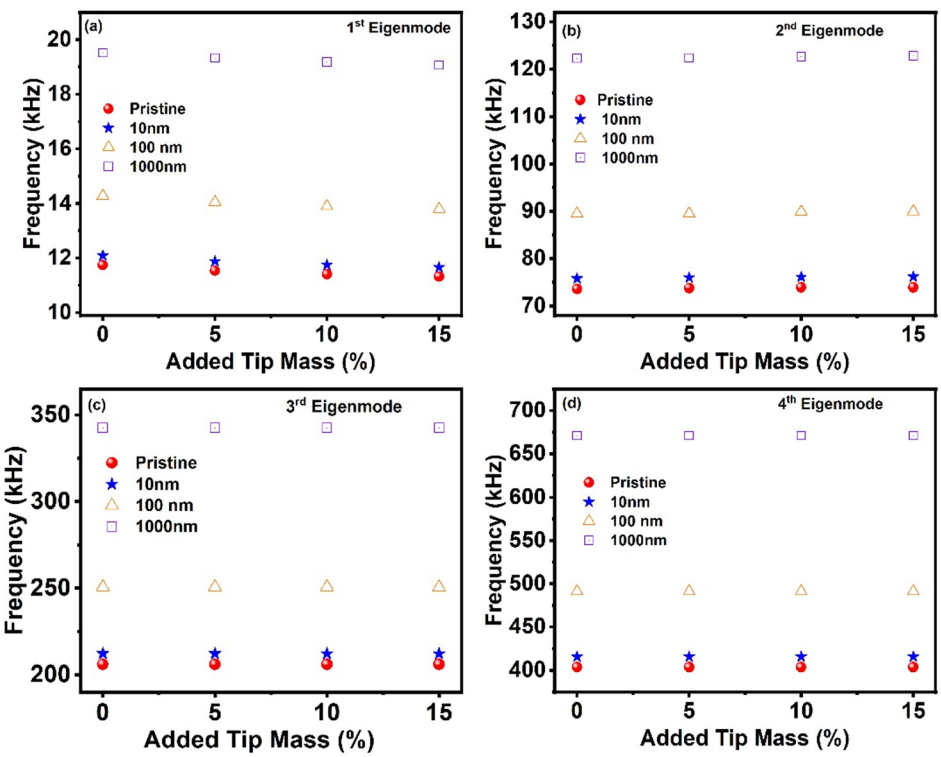

Fig. 2 Study of the effect of tip mass on the eigenfrequencies of a microcantilever with different coating thicknesses. (a) The first eigenfrequency, (b) second eigenfrequency, (c) third eigenfrequency and (d) fourth eigenfrequency. The thickness of the coating is varied from 10 nm to 1000 nm. Increasing the thickness of the coating leads to an increase in frequency as the coated material is MoS_2, which is stiffer than the cantilever material (here, silicon).

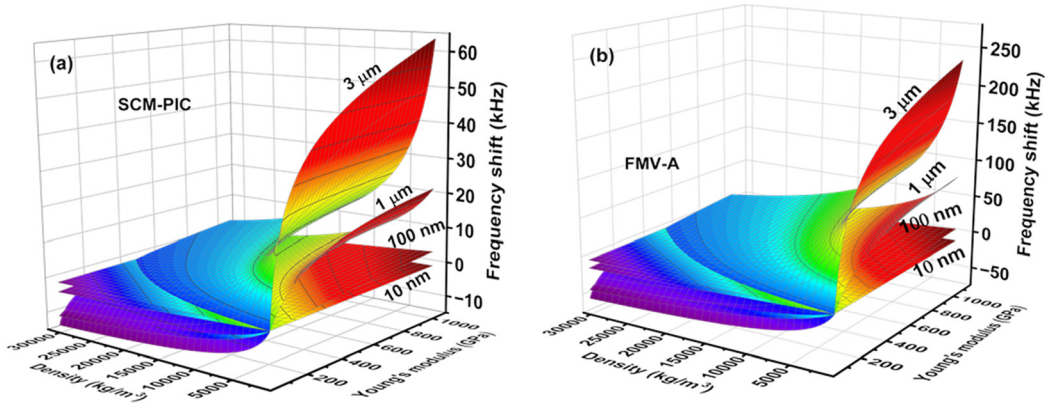

Fig. 3 3D plots obtained from the numerical simulation results of frequency shift due to the changes of Young's modulus and density of coated bulk materials on the microcantilever surface with different coating thicknesses for the SCM-PIC cantilever and the FMV-A cantilever. (a) The changes in frequency shift for the SCM-PIC cantilevers where the coating thicknesses were 10 nm, 100 nm, 1 μm, and 3 μm, respectively. (b) The changes in frequency shift for SCM-PIC cantilevers where the coating thicknesses were 10 nm, 100 nm, 1 μm, and 3 μm, respectively.

To summarize our simulations (Fig. 3 and Fig. S1, S2), we can mention that in our study, we simulated MoS_2 coating on three types of cantilevers:

- SCM-PIC (silicon): length 450 μm, thickness 2.5 μm, and spring constant ~0.2 N m^{-1}
- FMV-A (silicon): length 225 μm, thickness 2.5 μm, and spring constant ~2 N m^{-1}
- Quest R 200 (silicon nitride): length 200 μm, thickness 900 nm, and spring constant ~0.2 N m^{-1}

Despite SCM-PIC and Quest R200 having comparable stiffness (~0.2 N m^{-1}), the frequency shift upon MoS_2 deposition was consistently larger for Quest R200. This can be attributed to their significantly different effective masses. SCM-PIC is both longer and thicker than the Quest R200, which results in a higher effective mass. Since the relative frequency shift is governed by mass and stiffness changes, a higher cantilever mass leads to a smaller relative frequency shift. As a result, for the same MoS_2 coverage, Quest R200—with its smaller mass—undergoes a larger fractional frequency shift than SCM-PIC. Thus, even with similar stiffness, geometry and material differences lead to substantially different frequency responses.

The second silicon cantilever, FMV-A, further highlights this contrast. It has a slightly longer length (225 μm) than Quest R200 (200 μm) but is much stiffer (~2 N m^{-1}) and thicker (2.5 μm). Consequently, FMV-A exhibits the largest effective mass and lowest compliance changes among the three. As predicted by resonance theory, its frequency response to surface loading is minimal.

This is the prime reason for the highest frequency shift in the case of the QUEST R 200 cantilever. Furthermore, as can be seen from Fig. 3, S1 and S2 in SI, as we have used 2D materials with high Young's moduli, in most cases we observe positive frequency shifts, which can be related to the dominance of stiffness changes over mass changes in the deposited microcantilevers and by increasing the thickness of deposited materials, the positive frequency shift is increased.

In the subsequent step, we validate the analytical equations for calculating critical values (eqn (4a) and (4b)) by comparing them with the corresponding numerical simulation results. For this comparison, we focused on extreme case height scenarios, with the coated layer thickness considered at 10 nm and 3 μm, respectively.

The variations of critical density with Young's modulus and critical Young's modulus with density are calculated for the three cantilevers: (a) FMV-A and (b) QUEST R 200 (depicted in Fig. 4a–d), and (c) SCM-PIC (Fig. S3a and S3b).

The results reveal a remarkable alignment between numerical simulations and the analytical equations. Through this analysis, we observed that, for lower added layer thickness, the FMV-A cantilever achieved a critical density at a relatively higher value compared to the QUEST R 200 cantilever for the same coated Young's modulus (Fig. 4a). The variation is linear at lower heights but exhibits significant non-linearity for a thicker added layer (3 μm). Furthermore, for the thicker height, the behavior of both cantilevers reversed, with the FMV-A cantilever attaining a lower critical density than the QUEST R 200 cantilever at the same Young's modulus (Fig. 4b).

Concerning the critical Young's modulus for the low height of the added layer, similar to the critical density, we observed a linear relationship. For the same density of the added layer, the FMV-A cantilever reached the critical Young's modulus at a lower value (Fig. 4c). Although the cantilevers exhibited nonlinearity at a height of 3 μm, in this case, the QUEST R 200 cantilever reached the critical Young's modulus at a lower value compared to the FMV-A cantilever (Fig. 4d). The variations for the SCM-PIC cantilever are almost identical to those of the FMV-A cantilever (Fig. S3a and S3b) since both cantilevers share similar material properties.

Our analysis thoroughly explores the complex interaction of critical Young's modulus, density, and coating layer thickness, revealing a nonlinear coupling effect that impacts the direction of frequency shift in coated microcantilevers. Additionally, considering the different densities and Young's moduli of

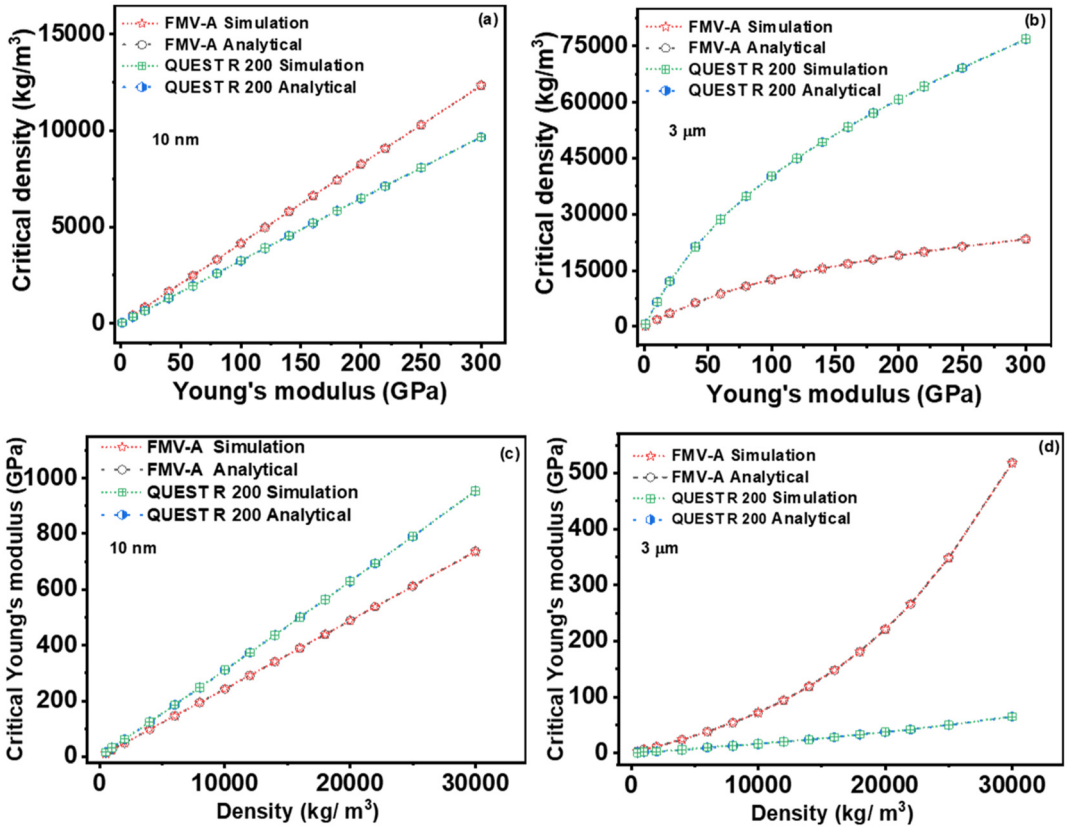

Fig. 4 Comparison between the critical density and Young's modulus obtained from numerical simulations and developed analytical equations. (a) and (b) The critical densities *vs.* Young's moduli for QUEST R 200 and FMV-A cantilevers for 10 nm and 3 μm added layer thicknesses, respectively. (c) and (d) the critical Young's moduli *vs.* densities for QUEST R 200 and FMV-A cantilevers for 10 nm and 3 μm added layer thicknesses, respectively.

silicon and silicon nitride as the materials of FMV-A and QUEST R 200 microcantilevers, this phenomenon is closely linked to the inherent stiffness and mass of the pristine microcantilever. Furthermore, our modeling approach and results can serve as a guideline for elucidating the anomalous frequency shifts observed in microcantilevers coated with various materials. This section can be summarized as:

The phenomenon of frequency shift polarity reversal arises from the interplay between two competing effects induced by the coating: (1) the added mass loading, which tends to *decrease* the resonance frequency, and (2) the effective stiffness enhancement, which tends to *increase* it. The net result of coating a cantilever depends on which of these two opposing contributions dominates.

When a thin film is deposited on the cantilever, the total mass increases due to the film's mass per unit area, which scales linearly with the density and thickness of the film. Simultaneously, the stiffness of the cantilever is altered, since the film also contributes to the bending rigidity of the composite structure. The degree of this enhancement depends on the Young's modulus and the film's position relative to the neutral axis and scales strongly with thickness.

Thus, a coating with high density and low Young's modulus will primarily increase the effective mass without contributing significantly to stiffness, resulting in a negative frequency shift (downshift). Conversely, a coating with high Young's modulus and relatively low density can increase stiffness more than the mass, yielding a positive frequency shift (upshift).

The combination of density and Young's modulus at which this crossover happens defines the critical values—the *critical density* and *critical Young's modulus*—for a given cantilever geometry and film thickness. This is why we observe a well-defined point of polarity reversal that is sensitive to the coating's mechanical properties and the cantilever's dimensions.

Having established the generality of our analytical model for bulk materials, we extended our investigation to the domain of 2D materials, which exhibit unique mechanical and electronic properties. To this end, we parameterized our simulation with the material properties—including Young's modulus, density, and interlayer distance—of several prominent 2D materials: tungsten diselenide (WSe_2), tungsten disulfide (WS_2), titanium disulfide (TiS_2), molybdenum diselenide ($MoSe_2$), graphene, and hexagonal boron nitride (hBN) (see their parameters we used in our simulation in the Materials and methods section). We then systematically calculated the fundamental eigenfrequency shift (f_1) as a function of the number of deposited layers for two distinct commercial cantilevers, the SCM-PIC and the FMV-A, to assess both the

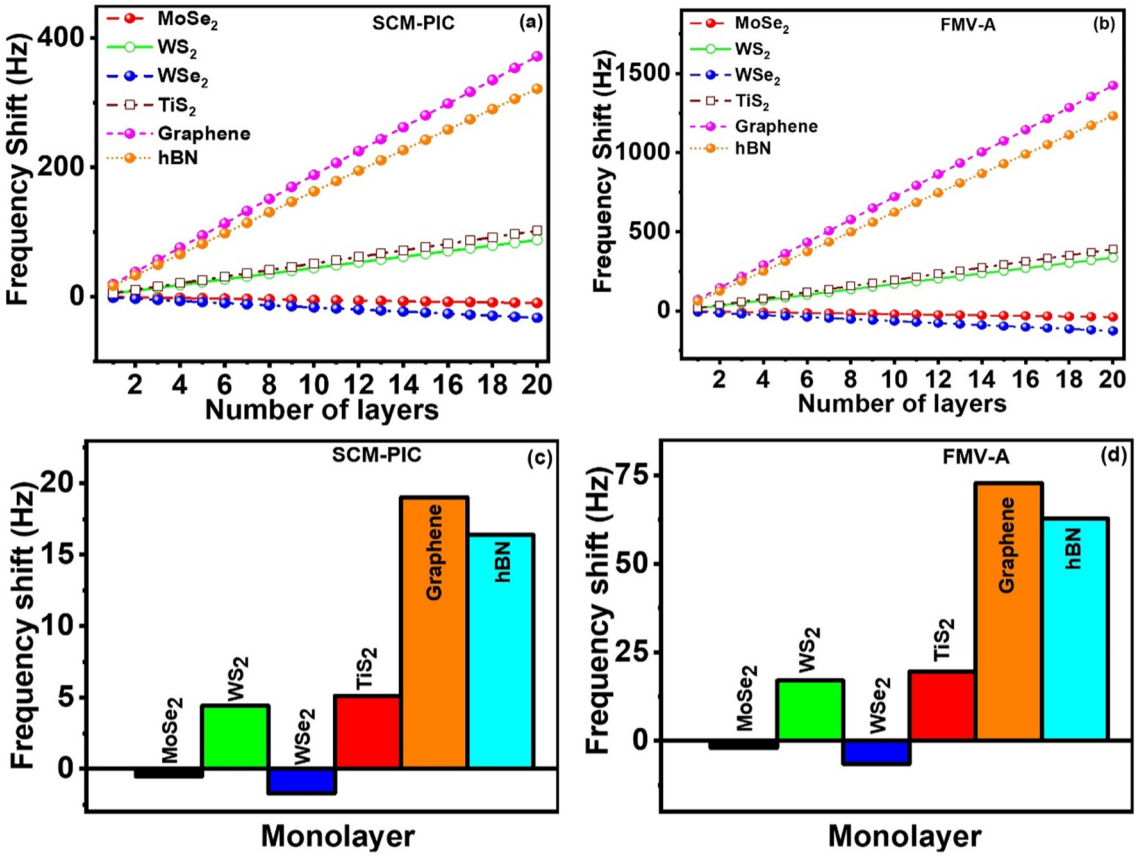

Fig. 5 (a) and (b) the frequency shifts of SCM-PIC and FMV-A cantilevers for different 2D materials and different numbers of 2D material layers. (c) and (d) the frequency shifts of SCM-PIC and FMV-A cantilevers for monolayer 2D materials.

material-dependent response and the cantilever sensitivity. The results of this comprehensive parametric sweep are presented in Fig. 5a and b, with a detailed analysis of the frequency shift for each specific 2D material as a function of layer number further provided in Fig. S4a and S4b in SI.

The simulations revealed a clear contrast in the cantilever response. For WS_2, TiS_2, graphene, and hBN, the eigenfrequencies of the modified cantilevers were higher than those of the pristine ones, indicating a positive frequency shift. In contrast, the frequencies of cantilevers coated with $MoSe_2$ and WSe_2 were lower, demonstrating a negative frequency shift. This can be explained by the dominance of mass changes over stiffness changes for $MoSe_2$ and WSe_2-coated microcantilevers, attributed to their lower Young's modulus and higher density compared to other materials.

To quantify this effect, we plotted the frequency shift for 20 layers of each material. For the SCM-PIC cantilever, positive frequency shifts of 87 Hz, 102 Hz, 372 Hz, and 322 Hz were observed for WS_2, TiS_2, graphene, and hBN, respectively. For $MoSe_2$ and WSe_2, negative frequency shifts of 10 Hz and 33 Hz were obtained. The FMV-A cantilever followed a similar trend but with a higher frequency shift, confirming its greater sensitivity. For the FMV-A, a 20-layer deposition of graphene yielded the highest positive frequency shift of 1.425 kHz, while WSe_2 produced the highest negative shift of 127 Hz. Positive shifts of 336 Hz, 390 Hz, and 1.23 kHz were observed for WS_2, TiS_2, and hBN, respectively, and a negative shift of 38 Hz was observed for $MoSe_2$.

The model's sensitivity extends to the monolayer limit, as detailed in Fig. 5c and d. For the SCM-PIC, the monolayer frequency shifts were +4.5 Hz (WS_2), +5 Hz (TiS_2), +16.4 Hz (hBN), and a maximum of +19 Hz for graphene, while $MoSe_2$ and WSe_2 produced negative shifts of −0.5 Hz and ∼−2 Hz, respectively. For the more sensitive FMV-A cantilever, the monolayer shifts were +18 Hz (WS_2), +20 Hz (TiS_2), +66 Hz (hBN), and a maximum of +72 Hz for graphene, with $MoSe_2$ and WSe_2 showing negative shifts of −2 Hz and ∼−7 Hz, respectively. These findings not only validate the predictive power of our model across diverse material systems but also provide a quantitative guide for selecting or synthesizing 2D materials to achieve a desired frequency response in coated microcantilevers.

Experimental section

We applied the developed equations to quantify the mass, thickness, number of layers, and Young's modulus of 2D materials. Additionally, we demonstrated our experimental approach for coating the microcantilever surface with 2D

materials to precisely control the cantilever's resonant frequency for sensing applications. In this context, we modified the SCM-PIC, PPP-NCH and TAP300DLC cantilevers by coating their surfaces with MoS_2 using the van der Waals epitaxy technique (VdWE), followed by a transfer process.[26,27,36] In our 2D material transfer process, we avoided using harsh chemicals to etch the substrate. Instead, we used only high-purity DI water to separate the 2D materials from the substrate (300 nm SiO_2/Si). Additionally, the 2D materials were supported with PS on a TR frame, ensuring that only the 2D materials/PS film came into contact with the cantilever. To remove PS, we used high-purity chloroform, which has the best solubility for PS, in a sealed container for 48 hours. This ensured no PS residue remained on the cantilevers. Finally, the cantilevers with the 2D materials were further rinsed with chloroform.

The as-grown MoS_2 samples were then characterized using HRTEM, Raman spectroscopy and X-ray photoelectron spectroscopy (XPS). The thickness and number of layers of the as-grown MoS_2 specimen were measured using HRTEM and are presented in Fig. 6a. Between 5 and 7 layers of MoS_2 sheets were observed, and a layer thickness of ~0.65 nm was measured, which matches nicely with the values reported in the literature.[37]

Raman spectroscopy is considered to be the fingerprint to obtain the number of layers of any MoS_2 sample. From the difference between the wavenumbers of the vibrational peaks corresponding to E_{2g} and A_{1g}, one can obtain valuable information about the number of layers corresponding to MoS_2. In our measurement, we recorded the Raman spectra utilizing a 532 nm laser system and considered different parts of the added layer on all three cantilevers. The average difference between the two peaks for the SCM-PIC cantilever is calculated to be ~24.3 ± 0.1 cm^{-1} (Fig. 6b). For the PPP-NCH and TAP300DLC cantilevers, the values are calculated to be ~24.1 ± 0.1 cm^{-1} and ~24.0 ± 0.1 cm^{-1}, respectively (Fig. S5a and S5b in SI). All these wavenumber shifts correspond to 5–7 layers.[38,39]

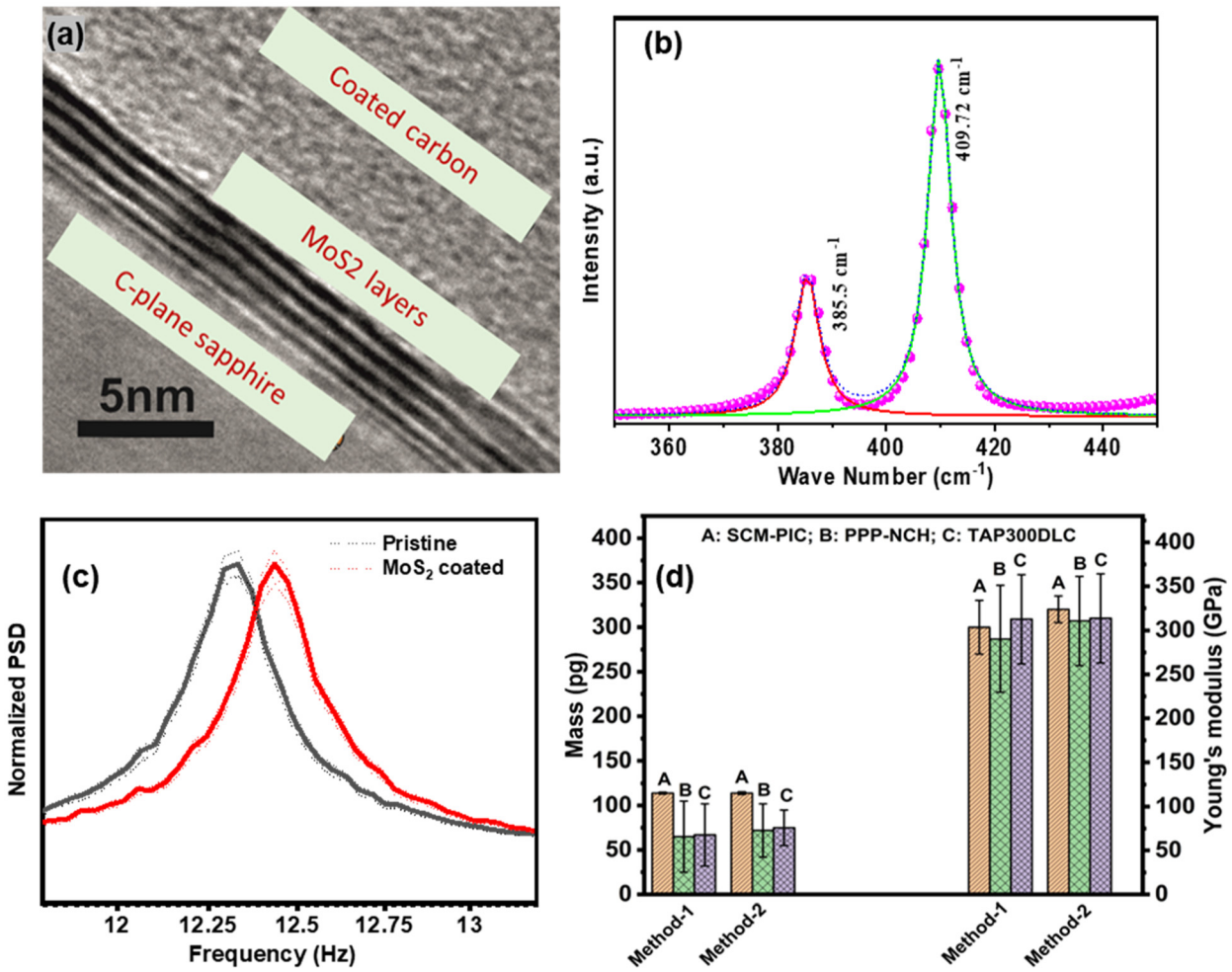

Fig. 6 (a) HRTEM image of the as-synthesized MoS_2 sample. (b) Raman spectrum of a few-layer MoS_2 coating on the SCM-PIC cantilever, highlighting the E_{2g} and A_{1g} vibrational bands. (c) Normalized thermal noise spectra of pristine SCM-PIC (black line) and MoS_2-coated SCM-PIC (red line) cantilevers highlighting the 1st eigenfrequencies of the cantilevers and (d) the measured values of mass (yellow bars) and Young's modulus (blue bars) of the deposited few layers of MoS_2 calculated using method 1 and method 2 for (A) SCM-PIC, (B) PPP-NCH, and (C) TAP300DLC cantilevers.

X-ray photoelectron spectroscopy (XPS) was carried out to characterize the compositions of these VdWE-grown MoS_2 layers to investigate two core levels, the Mo 3d and the S 2p of the as-synthesized MoS_2, and the results are presented in Fig. S6A(a) and S6A(b) in SI. As shown in Fig. S6A(a), two MoS_2 peaks (dark blue), Mo(IV) $3d_{3/2}$ and Mo(IV) $3d_{5/2}$, were found at 232.8 eV and 229.6 eV, respectively. In the same spectrum, the S 2s peak (pink) was observed at 226.8 eV, and the peak at 236.3 eV was assigned to Mo(VI) $3d_{3/2}$ (light blue), indicating a small amount of oxidation, which resulted from the sample being exposed to the ambient environment. It should be noted that a Mo(VI) $3d_{5/2}$ peak overlaps with Mo(IV) $3d_{3/2}$ at 232.8 eV. For the MoS_2 S 2p core level, two peaks (pink) labelled in Fig. S6A(b) as S $2p_{1/2}$ and S $2p_{3/2}$ corresponding to MoS_2 were found at 163.6 eV and 162.4 eV, respectively. In addition, with a semi-quantitative method to investigate the ratio of elements, the atomic ratio of S/Mo was found to be close to 2 with a slight S deficiency.

To further verify the extent and uniformity of the MoS_2 coating, we conducted field emission scanning electron microscopy (FESEM) combined with energy-dispersive X-ray spectroscopy (EDAX) (Fig. S6B in SI). Fig. S6B clearly shows the presence of molybdenum (Mo) and sulfur (S) across the surface of the originally Al-coated Si cantilever, confirming the spatial distribution of the coating.

To further assess the uniformity and thickness of the MoS_2 film, Raman spectroscopy was performed at multiple locations along the coated cantilevers (Fig. S6C in SI). The observed peak positions and inter-peak separations were consistent across different regions, indicating a uniform number of MoS_2 layers and confirming the reproducibility of the coating. The number of layers estimated from Raman spectra (5–7 layers) is in good agreement with our HRTEM analysis, which provides a direct measure of the MoS_2 thickness.

After preparing the MoS_2-coated microcantilevers, we measured the frequency response of the coated microcantilevers and compared them with their pristine counterparts. First, we implemented the methodology presented on the SCM-PIC cantilever, and then we extended that to PPP-NCH and TAP300DLC cantilevers.

The thermal noise spectra of pristine SCM-PIC and MoS_2-coated SCM-PIC cantilevers are recorded and plotted in Fig. 6c. The first eigenmode of the pristine and coated cantilevers was found to be 12.32 ± 0.05 kHz and 12.44 ± 0.02 kHz, respectively. In this case, we observed that the frequency of the pristine cantilever is lower than that of the coated cantilever, which shows the dominance of stiffness changes over mass changes when MoS_2 is coated on the microcantilever, which can be explained by the high Young's modulus of MoS_2.

As mentioned in the Introduction, to calculate the mass, Young's modulus and thickness of deposited MoS_2 on the microcantilevers, we have used two methods (Fig. 1b).

In the first method, by knowing the number of layers and the thickness of the coated MoS_2 from HRTEM and Raman spectroscopy measurements, we can calculate the mass of the coated MoS_2 microcantilevers from the geometrical parameters of the cantilever. The obtained mass from the geometrical parameters of the microcantilever (eqn (S5)) is 114 ± 0.5 pg. Then, we use eqn (1)–(3) to measure the Young's modulus of deposited MoS_2. The value we obtained is 305 ± 30 GPa (we called this as method 1).

In the second method, based on our approach that considers the variations of both stiffness and mass of the microcantilever due to the coating of the layer on its surface and our ability to measure the spring constant of the coated microcantilever, we use the following equation to not only measure the mass of deposited MoS_2 but also directly measure the number of layers of the 2D material using the microcantilever *via* decoupling the mass and stiffness changes effect from the measured frequency shift:

$$\Delta m = \frac{1}{4\pi^2}\left(\frac{k_N}{{f_N}^2} - \frac{k_{N+\Delta f_N}}{\left(f_N \pm \Delta f_N\right)^2}\right) \tag{7}$$

where k_N is the spring constant of the pristine cantilever and $k_{N+\Delta f_N}$ is the spring constant of the coated MoS_2 microcantilever. In eqn (7), f_N is the resonance frequency of the pristine cantilever and Δf_N is the frequency shift between the pristine and modified cantilevers.

The mass of deposited MoS_2 is calculated to be 114 ± 0.2 pg, which corresponds to 5 to 7 layers of MoS_2 and is the same as the value we obtained by knowing the number of layers from HRTEM and Raman spectroscopy. It not only proves the accuracy of the presented methodology but also depicts the capability of microcantilevers to directly measure the number of layers of 2D materials.

It is worth mentioning that the measured spring constants of pristine and MoS_2-coated microcantilevers are 0.16 ± 0.06 N m^{-1} and 0.17 ± 0.05 N m^{-1}, respectively.

By measuring the spring constant of the MoS_2-coated microcantilever, we can use eqn (S4) (SI) as well as eqn (2) and (3) to measure the Young's modulus of deposited MoS_2 (we called this approach method 2). The obtained value is 315 ± 15 GPa, which is similar to the values calculated from method 1 and matches well with the reported values in the literature.[40–42]

To show the generality and repeatability of our measurement, we then used the other two MoS_2-coated cantilevers (PPP-NCH and TAP300DLC) and measured the mass and Young's modulus of the added MoS_2 layer. The mass of the added MoS_2 layer for the PPP-NCH cantilever was found to be 65 ± 40 pg (method 1) and 72 ± 30 pg (method 2). Similarly, the mass obtained from the TAP300DLC cantilever was calculated to be 67 ± 35 pg (method 1) and 75 ± 20 pg (method 2). The Young's modulus of the added MoS_2 layer for the PPP-NCH cantilever was found to be 287 ± 60 GPa (method 1) and 309 ± 50 GPa (method 2). Accordingly, the Young's modulus obtained from the added MoS_2 layer for the TAP300DLC cantilever was calculated to be 307 ± 5 (method 1) and 310 ± 50 GPa (method 2).

The mass of deposited MoS_2 obtained from measuring the number of layers from HRTEM, Raman spectroscopy (method

1) and eqn (7) (method 2) is given in Fig. 6d (yellow bars). Also, the obtained Young's moduli of the MoS_2 coating from eqn (1)–(3) by knowing the number of layers from HRTEM and Raman spectroscopy (method 1) and also from eqn (7) and eqn (S4) (method 2) are given in Fig. 6d (blue bars).

To quantify the mass, number of layers and Young's modulus of deposited MoS_2 layers, the geometrical parameters of cantilevers would be involved. Due to the variations of the actual length, width and height of microcantilevers from their nominal values provided by manufacturers, we have performed integrated simulation–experimental analysis to probe the effects of their variations on the measured frequency response and frequency shift of both pristine and modified cantilevers. For this analysis, we utilized the three different cantilevers: (a) SCM-PIC, (b) FMV-A, and (c) PPP-NCH, with their nominal values provided in the Materials and Methods section. In the subsequent step, we measured their actual dimensions using Scanning Electron Microscopy (SEM) and consequently determined their resonance frequency *via* thermal noise spectra analysis (see Fig. S7). It is worth mentioning that the spring constants were calibrated from the thermal noise spectra as well, using Sader's method.[43]

In our simulation, we assessed the impact of dimensional variations on the cantilevers, considering a maximum length change of 10% of their nominal length, a maximum width change of 33% of their nominal width, and a maximum thickness change of 25% of their nominal thickness. These variations are significantly higher than the actual measured changes.[44] We then analyzed the frequency changes resulting from these dimensional variations for both the pristine and the modified cantilevers. The resonance frequencies at nominal values, as well as the shifts due to dimension variations, are depicted in Fig. S7. The figure clearly illustrates that while the frequencies of both pristine and modified cantilevers are influenced by dimensional variations, the frequency shift caused by the added MoS_2 layer remains relatively constant across all variations.

Furthermore, in our quantification of the mass, number of layers, and Young's modulus of the MoS_2 layer coating, presented in Fig. 6d, we included error bars to account for uncertainties in the cantilever geometry used in the quantification.

It is noteworthy that for all our thermal noise measurements and simulations, we specifically opted for the nominal values of cantilevers rather than their actual values. As mentioned, in our analysis, we explored the deviations of cantilever dimensions from their nominal values and tracked their resonance frequencies accordingly. Furthermore, Fig. S7d (SI) provides a comprehensive plot depicting the percentage changes in frequency corresponding to percentage changes in height, specifically for the PPP-NCH cantilever. We used a similar approach in determining the frequency shifts as a function of the deviation of other dimensions for all the cantilevers.

To complement our simulation findings, we conducted experimental measurements of several cantilevers using scanning electron microscopy (SEM). These measurements revealed that the actual dimensions of all examined cantilevers fell within the range of deviations considered in our simulation methodology. Highlighting the real dimensions of the PPP-NCH cantilever, Fig. S7e and S7f (SI) present a representative SEM image. The measured length and width of this cantilever were found to be 132.5 μm and 40.2 μm, respectively, while the thickness was found to be 3.8 μm.

Furthermore, it is worth mentioning that in our error analysis, we considered a range of measured layers of MoS_2 by HRTEM and Raman spectroscopy, variations in the measured frequency and spring constant before and after deposition using thermal spectra, as well as the error range in the cantilever parameters as discussed above. For this reason, we provide the average and max/min values for measured mass and Young's modulus.

Next, to show and compare the performance of our proposed MoS_2-coated microcantilevers in sensing applications, we have used our modified microcantilevers to measure the mass of antibiotic-resistant (ABR) *E. coli* bacteria as well as different concentrations of uric acid.

It should be noted that in our sensing experiments, we follow our previous work,[25] in which the cantilever was not fully immersed in liquid during these experiments. Instead, a thin droplet of PBS buffer was carefully placed atop the cantilever surface, resulting in a thin liquid film on the surface of the cantilever rather than full submersion. Because of this, the added mass and hydrodynamic loading from the bulk liquid are minimal compared to full immersion scenarios.

For the measurement of the mass of ABR *E. coli*, we grew a culture of ABR *E. coli* and resuspended the bacteria in a phosphate-buffered saline (PBS) buffer solution. To determine the mass of *E. coli*, we first considered the effect of the PBS layer. In our experimental setup, we deposited 5 μl of PBS on both cantilevers. In the next step, we deposited 5 μl of the bacteria suspended in PBS over the pristine and modified cantilever and for all the cases, we monitored the 1st eigenfrequencies obtained from the thermal noise spectra (Fig. 7a and b). The concentration of *E. coli* was determined *via* a plate count method with an average of 5416 ± 861 colony-forming units (CFU), and the reported mass of an *E. coli* cell is 1048 ± 98 fg (~1 pg);[28] therefore, the mass of the sample is estimated to be ~5.416 ± 0.861 ng.

In this part of our measurement, first, we use the pristine and modified SCM-PIC cantilevers as potential mass sensors to quantify the mass of *E. coli* effectively and accurately.

In the case of the pristine cantilever, we observed a 3 Hz negative frequency shift when PBS was deposited on the top of the cantilever. For the same amount of PBS, the MoS_2-coated cantilever exhibited a higher negative frequency shift of ~7 Hz. This confirms that the responsivity of the MoS_2-coated cantilever is higher than that of the pristine cantilever, which can provide a more trustworthy frequency shift for the added PBS layer.

From Fig. 7a and b and Fig. S8(a–d) (SI), we observed a substantial frequency shift from the natural frequency of PBS layer-modified cantilevers. Frequency shifts of 75 Hz and 116 Hz (equivalent to 0.7% and 1% relative frequency shifts) were obtained from the pristine and MoS_2-coated SCM-PIC cantilevers, respectively.

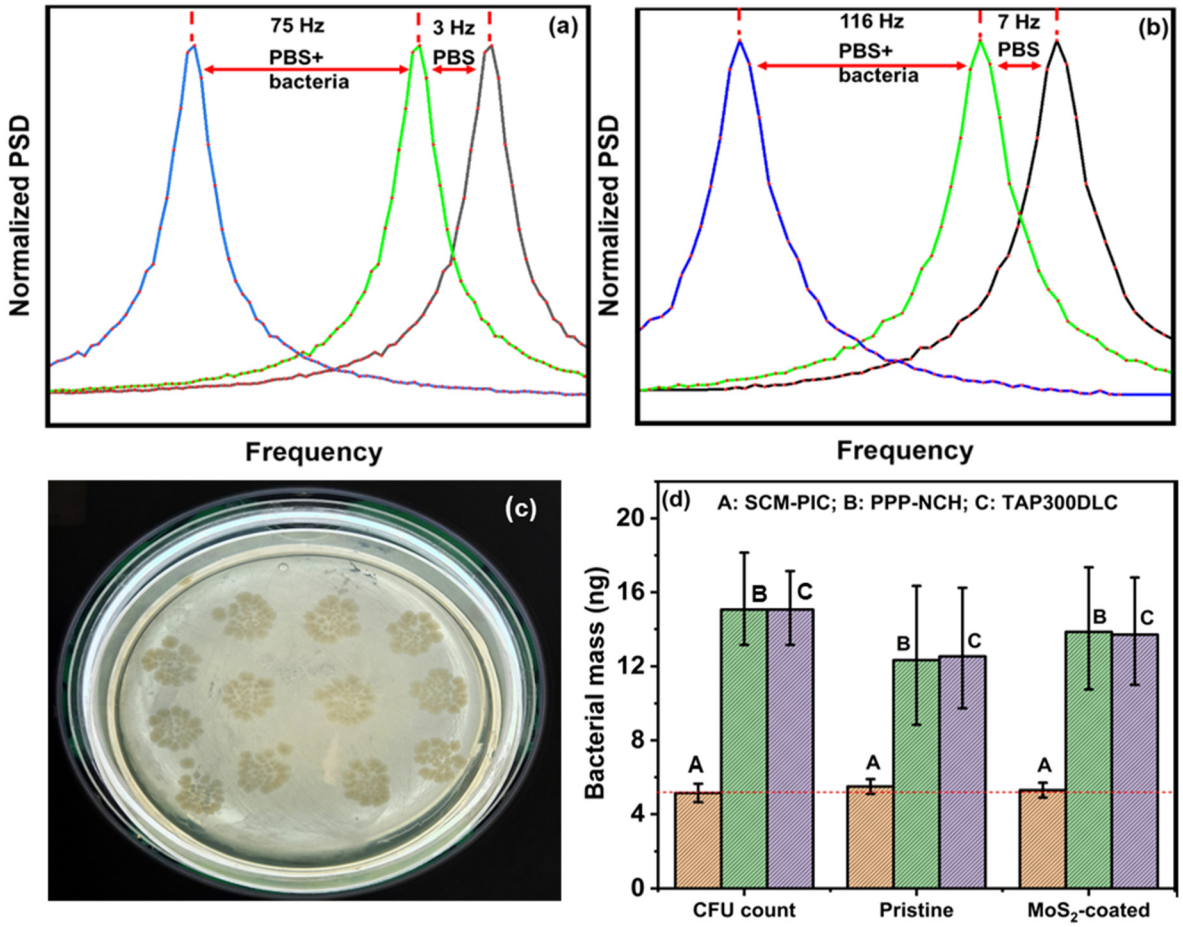

Fig. 7 (a) Thermal noise spectra for the pristine SCM-PIC cantilever in air, with PBS buffer, and with *E. coli* bacteria in PBS. The first eigenfrequency of the pristine cantilever in the air was found to be 11.413 kHz. (b) Thermal noise spectra for the MoS_2-coated SCM-PIC cantilever in air, with PBS buffer, and with *E. coli* bacteria in PBS. The first eigenfrequency of the pristine cantilever in the air was found to be 12.444 kHz (air = black, PBS buffer = green, and *E. coli* bacteria in PBS = blue). (c) Bacterial colony in the agar plate. (d) The calculated mass of the *E. coli* bacteria from the CFU count and the frequency shift for pristine and MoS_2-coated cantilevers ((A) SCM-PIC (orange), (B) PPP-NCH (green) and (C) TAP300DLC (purple)).

We then used eqn (7) to determine the mass of the bacteria for both the cantilevers and compared the as-obtained mass from the CFU counts. The masses obtained by the CFU measurement and from the frequency shift data for both the cantilevers are very close to each other, while the modified microcantilever shows superior precision (Fig. 7d). Our results demonstrated that the mass of the added bacteria can be measured effectively and accurately, indicating that the proposed 2D material-coated microcantilever functions as a highly responsive mass sensor.

Similar analyses were carried out using the PPP-NCH and the TAP300DLC cantilever (pristine and coated). The thermal noise spectra of all four cantilevers (two pristine and two modified) are presented in Fig. S8(a–d). In this case, the mass of the *E. coli* bacteria obtained from the plate counts was calculated to be ~15.016 ± 3.0 ng. The resonance frequencies of the cantilevers were found to be 310.1 kHz (PPP-NCH), 313.67 kHz (MoS_2-coated PPP-NCH), 295.32 kHz (TAP300DLC) and 297.48 kHz (MoS_2-coated TAP3000DLC). Here also, we observed negative frequency shifts of 80 Hz (PPP-NCH), 176 Hz (MoS_2-coated PPP-NCH), 76 Hz (TAP300DLC) and 168 Hz (MoS_2-coated TAP3000DLC) when PBS was deposited on the top of the cantilevers.

On the other hand, frequency shifts of 9.1 kHz and 13.8 kHz (3% and 4.4% relative frequency shifts) were measured, respectively, for pristine and MoS_2-coated PPP-NCH cantilevers. Similarly, frequency shifts of 8.7 kHz and 11.68 kHz (2.94% and 3.92% relative frequency shifts) were measured respectively for pristine and MoS_2-coated TAP300DLC cantilevers. The significant changes in frequency shifts for these two types of cantilevers can be explained by their significantly higher frequencies and shorter length.

For these cantilevers as well, we observed that the responsivity of the modified cantilevers is greater than that of the pristine cantilever. Moreover, the obtained negative frequency shifts highlight the dominance of mass changes over stiffness changes in the microcantilever when PBS is added to its surface.

Uric acid plays multifaceted roles as a crucial biomarker, neurotransmitter, and antioxidant, necessitating its precise detection in bodily fluids. In the concluding phase of this

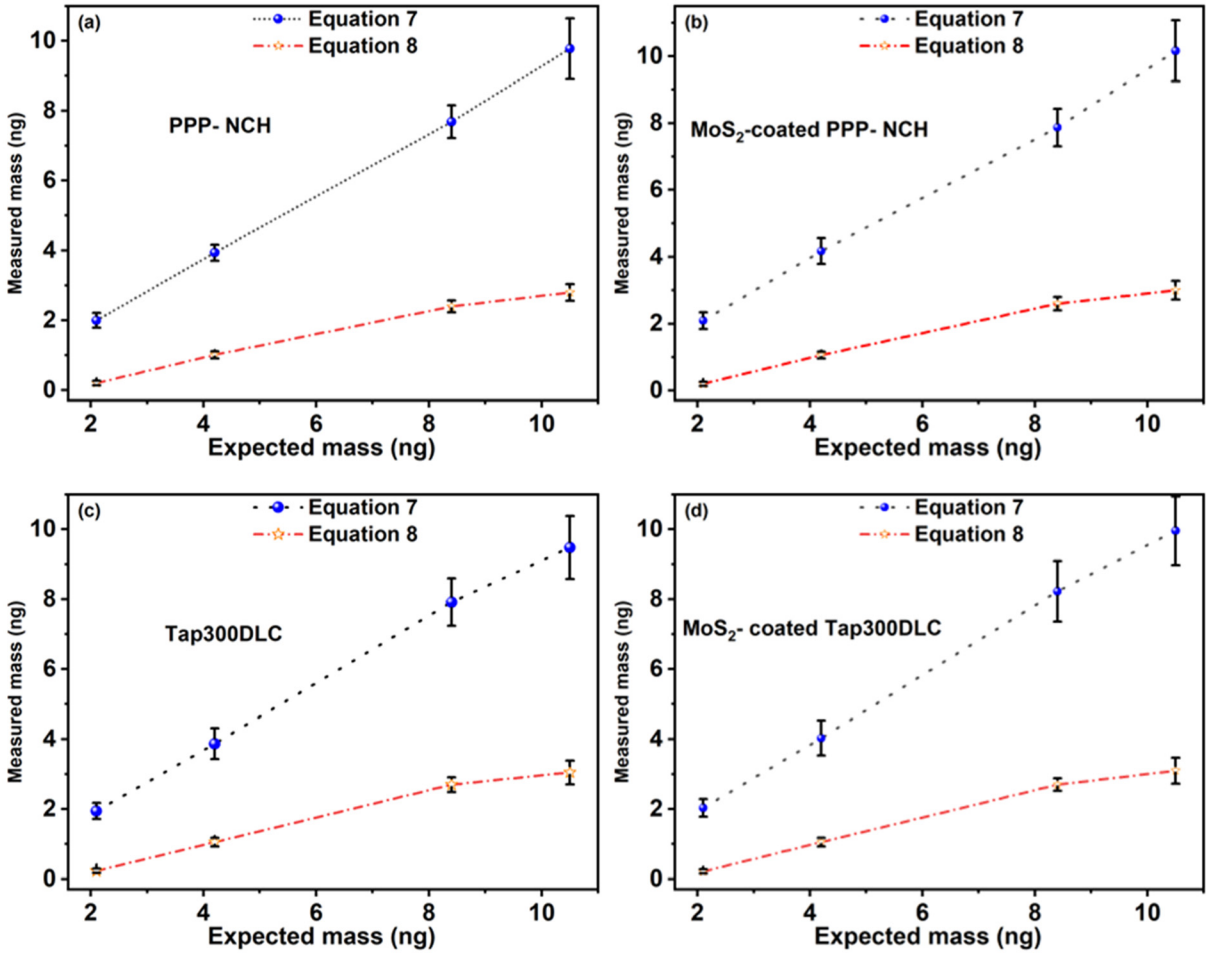

Fig. 8 Variation of expected mass (calculated from concentration) and measured mass calculated from the (a) PPP-NCH cantilever, (b) MoS_2-coated PPP-NCH cantilever, (c) TAP300DLC cantilever and (d) MoS2-coated TAP300DLC cantilever using two different mathematical equations for uric acid.

investigation, our aim was to detect different concentrations of uric acid dissolved in PBS solution, ranging from 2 μM to 15 μM. We used both the pristine and MoS_2-coated cantilevers (PPP-NCH and TAP300DLC) and measured the resonance frequencies and the corresponding spring constant. Then, we employed two distinct mathematical methodologies (eqn (7) and (8)) to ascertain the mass of uric acid molecules.

It is worth mentioning that eqn (8) is a conventional equation mostly used to measure the mass by a cantilever.[45,46]

$$\Delta m = \frac{k_N}{4\pi^2}\left(\frac{1}{{f_N}^2} - \frac{1}{(f_N - \Delta f_N)^2}\right) \quad (8)$$

The variation between the measured and the expected mass (calculated based on concentration) is delineated in Fig. 8. Once again, our mathematical model provided a more precise estimation of mass, while the model derived from the literature failed to accurately gauge the mass of uric acid molecules, resulting in an underestimated mass value. Here, we also found that the modified cantilever is capable of measuring the mass of uric acid molecules more accurately than the pristine cantilever, and we also observed that the MoS_2-coated PPP-NCH cantilever is capable of measuring the mass of uric acid more precisely and accurately than the MoS_2-coated TAP300DLC cantilever.

Conclusion

In summary, we have employed a theoretical and simulative model to analyze the effect of the coating layer on the frequency response of cantilevers. Subsequently, we presented a deposition methodology to coat the cantilever surface with 2D materials *via* the van der Waals Epitaxy (VdWE) approach. We demonstrate the capability of our developed methodology to measure the mass, thickness, number of layers and Young's modulus of 2D materials. Furthermore, following the digital twin concept, our proposed approach can precisely control the characteristics of 2D material-coated microcantilevers and benefit from the exotic properties of 2D materials for sensing applications requiring highly sensitive detection characteristics. We demonstrate that the developed MoS_2-coated cantilever has

higher responsivity than its pristine counterpart, which offers higher accuracy in mass spectrometry measurements.

Materials and methods

AFM probe

We employ the Asylum Research Oxford Jupiter AFM system to assess the natural frequencies and the spring constants of all the cantilevers under ambient conditions. The specific cantilevers utilized for our experimental measurement are (a) SCM-PIC (Nanoworld, Switzerland) with nominal dimensions: length: 450 μm, width: 50 μm, and thickness: 2.5 μm, (b) PPP-NCH (Nanosensors Switzerland) with nominal dimensions: length: 125 μm, width: 30 μm and thickness: 4 μm and (c) TAP300DLC (Budget Sensor, Bulgaria) with nominal dimensions: length: 125 μm, width: 30 μm and thickness: 4 μm.

Deposition of MoS_2 on cantilevers

The MoS_2 2D layers were fabricated on a Si wafer with a 300 nm SiO_2 layer (300 nm SiO_2/Si) or a *c*-plane sapphire substrate by van der Waals Epitaxy (VdWE).[26,27,36,47] The VdWE-grown few-layer MoS_2 on the 300 nm SiO_2/Si substrate was spin-coated with 7% polystyrene (PS, Sigma-Aldrich) in toluene at a speed of 1000 rpm for 50 s, and then baked on a hot plate at 90 °C for 15 min. The coated sample was subsequently attached to a supporting frame made with thermal release (TR) tape (from Nitto). Then, the TR frame/PS/MoS_2/300 nm SiO_2/Si was immersed in DI water to allow water to penetrate through the van der Waals gap between MoS_2 and the 300 nm SiO_2/Si substrate. After that, the TR frame/PS/MoS_2 floated on the DI water and was then further rinsed with DI water. The TR frame/PS/MoS_2 was ready for transfer on cantilevers, and then the TR frame was released by baking at 110 °C for 30 min. Finally, the PS layer was removed by immersing it in chloroform.

Characterization

The High-Resolution Transmission Electron Microscope (HRTEM) images were obtained using a JEOL 3010 transmission electron microscope. The Raman spectra were acquired employing a Renishaw inVia Raman spectrometer, utilizing a 532 nm laser, with an exposure time of 30 seconds and a laser power of 25 mW. X-ray photoelectron spectroscopy (XPS) was carried out by using a Thermo Scientific Theta Probe XPS System. The thermal noise data obtained from both cantilevers were employed for the determination of the individual eigenmodes of the cantilevers. The scanning electron microscope images of the PPP-NCH cantilever were captured using a Hitachi SU5000 field-emission scanning electron microscope (FESEM).

Bacterial growth

Isolation and identification of antibiotic-resistant (ARB) *E. coli*. *E. coli* was isolated from effluent samples collected at Carrickfergus Wastewater Treatment Works, Belfast, UK. The effluent was plated on selective Chromocult coliform agar, using membrane filtration following ISO 9308-1. The antibiotic resistance (ABR) of *E. coli* was tested against Trimethoprim (TMP), Sulfamethoxazole (SMX), Ofloxacin (OFX), Ampicillin (AMP), Tetracycline (TET) and Ciprofloxacin (CIP) to the minimum inhibitory concentration stated by the European Committee on Antimicrobial Susceptibility Testing (EUCAST) and Clinical Laboratory Standards Institute (CLSI). The standard protocol for freezing bacteria using glycerol (15%) and cryobeads was employed to maintain viable ARB *E. coli* stock in sterile tubes for further tests.

Microbial culture and analysis. A stock plate of ABR *E. coli* was prepared using the frozen strains of ABR *E. coli*. The sample was taken from a freezer, and a fresh culture was prepared using tryptic soy broth (TSB) inoculated with 2 single cryobeads and incubated at 37 °C for 21 h under constant agitation at 120 rpm in an orbital rotary shaker. An inoculation loop was then used to streak *E. coli* from the TBS broth onto Chromocult coliform agar, which was stored at 4 °C in a fridge. A new stock was prepared each month to maintain similar experimental conditions for bacterial testing.

Culture and suspension of *E. coli* in PBS. *E. coli* was grown in TSB inoculated with 2 colonies from a stock plate using an inoculated loop and incubated at 37 °C for ~21 h under constant agitation at 120 rpm in an orbital rotary shaker overnight so that the bacteria were in the stationary growth phase. The bacterial broth was then centrifuged at 4000 rpm for 1 min to form a pellet. After the supernatant was removed, the pellet was resuspended in 10 ml of phosphate-buffered saline (PBS). The original sample (~10^8 CFU ml^{-1}) was then diluted *via* serial 10-fold dilutions (twice) with PBS to a concentration of ~10^6 CFU ml^{-1}.

Enumeration of microorganisms. Serial dilutions (10-fold) were performed using PBS. For each dilution, six drops of 10 μL were plated on tryptic soy agar (TSA) and incubated at 37 °C for >18 h. Then, the plate dilution with a suitable number of countable colonies was enumerated, and the average and associated deviation were calculated for a 5 μl sample.

Uric acid solution. Uric acid and PBS tablets of analytical reagent (AR) grade were purchased from Sigma-Aldrich (UK) and were utilized without further purification. A 0.1 M PBS solution was prepared by dissolving the PBS tablets in ultrapure deionized (DI) water obtained from the Millipore Milli-Q system, with an electrical resistivity of 18 MΩ. A stock solution of 50 μM uric acid was prepared and subsequently diluted using the PBS buffer to attain the desired concentration.

Simulations. In our simulation using MATLAB software, we have considered that the different layers of the 2D materials are deposited on our pristine cantilever. For the sake of our calculation, in this present study, we have utilized three different commercial cantilevers: (a) SCM-PIC, (b) FMV-A and (c) QUEST R 200. The dimensions of the cantilevers are (a) SCM-PIC: length 450 μm, width 50 μm and thickness 2.5 μm and (b) FMV-A: length 225 μm, width 30 μm and thickness 2.5 μm and (c) QUEST R 200: length 200 μm, width 30 μm and thickness 0.9 μm. The spring constants of both cantilevers are 0.2 N $m^{-1,}$ 1.75 N m^{-1} and 0.2 N m^{-1}, respectively.

Table 1 Tabulated physical properties of $MoSe_2$, WS_2, WSe_2, TiS_2, hBN, and graphene. The table lists the interlayer spacing, density, and in-plane Young's modulus, with data sourced from the indicated (ref. 48–58)

Sample	Interlayer spacing (nm) (ref. 48, 49 and 50)	Density (kg m^{-3}) (ref. 51–53)	Young's modulus (GPa) (ref. 54–58)
$MoSe_2$	0.646	6900	154
WS_2	0.618	7500	302
WSe_2	0.651	8660	167
TiS_2	0.569	3220	228
hBN	0.335	2100	866
Graphene	0.335	2267	1000

In the simulation work, we have considered 6 different 2D materials, which are (1) molybdenum diselenide ($MoSe_2$), (2) tungsten disulfide (WS_2), (3) tungsten diselenide (WSe_2), (4) titanium disulfide (TiS_2), (5) graphene, and (6) hexagonal boron nitride (hBN).

The interlayer spacing, density and Young's modulus of all the above-mentioned 2D materials are tabulated in Table 1.

Conflicts of interest

The authors declare no conflicts of interest.

Data availability

The data supporting the findings of this study are available in the main manuscript and its supplementary information (SI). If additional data are required, we are happy to provide them as SI. Supplementary information: theoretical models, simulation results, and experimental data. Additional data, including raw frequency shift measurements, Young's modulus estimations, and mass sensing results for bacterial and uric acid concentrations, have also been included. See DOI: https://doi.org/10.1039/d5nr03147h.

Acknowledgements

This work was supported by the Department for the Economy (DfE), Northern Ireland, through US–Ireland R&D partnership grant no. USI 186, and the Engineering and Physical Sciences Research Council (EPSRC) grants EP/N00762X/1, EP/V040030/1, and EP/Y003551/1. The authors would like to thank Dr He Wang for the XPS measurement and Dr Shuncai Wang for the TEM measurement.

References

1 A. F. Payam and A. Passian, Imaging beyond the surface region: Probing hidden materials via atomic force microscopy, *Sci. Adv.*, 2023, **9**, 1–19.
2 S. S. Azadeh, *et al.*, Microcantilever-integrated photonic circuits for broadband laser beam scanning, *Nat. Commun.*, 2023, **14**, 2641.
3 A. Glia, M. Deliorman and M. A. Qasaimeh, 3D Generation of Multipurpose Atomic Force Microscopy Tips, *Adv. Sci.*, 2022, **9**, 1–15.
4 T. Liu, *et al.*, Ballistic dynamics of flexural thermal movements in a nanomembrane revealed with subatomic resolution, *Sci. Adv.*, 2022, **8**, 1–5.
5 J. Tamayo, P. M. Kosaka, J. J. Ruz, Á.S Paulo and M. Calleja, Biosensors based on nanomechanical systems, *Chem. Soc. Rev.*, 2013, **42**, 1287–1311.
6 J. L. Arlett, E. B. Myers and M. L. Roukes, Comparative advantages of mechanical biosensors, *Nat. Nanotechnol.*, 2011, **6**, 203–215.
7 A. K. Gupta, *et al.*, Anomalous resonance in a nanomechanical biosensor, *Proc. Natl. Acad. Sci. U. S. A.*, 2006, **103**, 13362–13367.
8 Y. Zhao, *et al.*, Achieving Ultrasensitivity and Long-Term Durability Simultaneously for Microcantilevers Inspired by a Scorpion's Circular Tip Slits, *ACS Nano*, 2022, **16**, 18048–18057.
9 I. Incaviglia, *et al.*, Tailoring the Sensitivity of Microcantilevers To Monitor the Mass of Single Adherent Living Cells, *Nano Lett.*, 2023, **23**, 588–596.
10 Y. Liu, Y. Tian, C. Lin, J. Miao and X. Yu, A monolithically integrated microcantilever biosensor based on partially depleted SOI CMOS technology, *Microsyst. Nanoeng.*, 2023, **9**, 60.
11 M. S. Hanay, *et al.*, Inertial imaging with nanomechanical systems, *Nat. Nanotechnol.*, 2015, **10**, 339–344.
12 S. Stassi, *et al.*, Large-scale parallelization of nanomechanical mass spectrometry with weakly-coupled resonators, *Nat. Commun.*, 2019, **10**, 3647.
13 P. M. Kosaka, *et al.*, Detection of cancer biomarkers in serum using a hybrid mechanical and optoplasmonic nanosensor, *Nat. Nanotechnol.*, 2014, **9**, 1047–1053.
14 E. Gil-Santos, *et al.*, Nanomechanical mass sensing and stiffness spectrometry based on two-dimensional vibrations of resonant nanowires, *Nat. Nanotechnol.*, 2010, **5**, 641–645.
15 M. Li, H. X. Tang and M. L. Roukes, Ultra-sensitive NEMS-based cantilevers for sensing, scanned probe and very high-frequency applications, *Nat. Nanotechnol.*, 2007, **2**, 114–120.
16 Y. T. Yang, C. Callegari, X. L. Feng, K. L. Ekinci and M. L. Roukes, Zeptogram-scale nanomechanical mass sensing, *Nano Lett.*, 2006, **6**, 583–586.
17 M. S. Hanay, *et al.*, Single-protein nanomechanical mass spectrometry in real time, *Nat. Nanotechnol.*, 2012, **7**, 602–608.
18 M. Sansa, *et al.*, Optomechanical mass spectrometry, *Nat. Commun.*, 2020, **11**, 1–7.
19 G. Bhattacharya, I. Lionadi, A. Stevenson, J. Ward and A. F. Payam, Tailored Microcantilever Optimization for Multifrequency Force Microscopy, *Adv. Sci.*, 2023, **2303476**, 1–11.
20 P. V. Gorelkin, *et al.*, Synthetic sialylglycopolymer receptor for virus detection using cantilever-based sensors, *Analyst*, 2015, **140**, 6131–6137.

21 L. Wang, *et al.*, Rapid and ultrasensitive electromechanical detection of ions, biomolecules and SARS-CoV-2 RNA in unamplified samples, *Nat. Biomed. Eng.*, 2022, **6**, 276–285.
22 J. Chaste, *et al.*, A nanomechanical mass sensor with yoctogram resolution, *Nat. Nanotechnol.*, 2012, **7**, 301–304.
23 H. Y. Chiu, P. Hung, H. W. C. Postma and M. Bockrath, Atomic-scale mass sensing using carbon nanotube resonators, *Nano Lett.*, 2008, **8**, 4342–4346.
24 A. Pallandre, B. De Meersman, F. Blondeau, B. Nysten and A. M. Jonas, Tuning the orientation of an antigen by adsorption onto nanostriped templates, *J. Am. Chem. Soc.*, 2005, **127**, 4320–4325.
25 G. Bhattacharya, *et al.*, Mass and Stiffness Deconvolution in Nanomechanical Resonators for Precise Mass Measurement and In Vivo Biosensing, *ACS Nano*, 2024, **18**, 20181–20190.
26 J. F. Felix, *et al.*, A comprehensive study on the effects of gamma radiation on the physical properties of a two-dimensional WS2 monolayer semiconductor, *Nanoscale Horiz.*, 2020, **5**, 259–267.
27 C. C. Huang, *et al.*, Facilitating Uniform Large-Scale MoS2, WS2Monolayers, and Their Heterostructures through van der Waals Epitaxy, *ACS Appl. Mater. Interfaces*, 2022, **14**, 42365–42373.
28 Y. Nan, D. Tan, J. Shao, M. Willatzen and Z. L. Wang, 2D Materials as Effective Cantilever Piezoelectric Nano Energy Harvesters, *ACS Energy Lett.*, 2021, **6**, 2313–2319.
29 J. Lee, *et al.*, Electrically tunable single- and few-layer MoS2 nanoelectromechanical systems with broad dynamic range, *Sci. Adv.*, 2018, **4**, 27–35.
30 B. Aidi, M. Shaat, A. Abdelkefi and S. W. Case, Free vibration analysis of cantilever open-hole composite plates, *Meccanica*, 2017, **52**, 2819–2836.
31 N. G. Stephen, Beam vibration under compressive axial load-upper and lower bound approximation, *J. Sound Vib.*, 1989, 345–350.
32 R. Whiting, M. A. Angadi and S. Tripathi, Evaluation of elastic moduli in thin-film/substrate systems by the two-layer vibrating reed method, *Mater. Sci. Eng. B*, 1995, **30**, 35–38.
33 E. Zgheib, A. Alhussein, M. F. Slim, K. Khalil and M. François, Multilayered models for determining the Young's modulus of thin films by means of Impulse Excitation Technique, *Mech. Mater.*, 2019, **137**, 103143.
34 H. Cho, Y. Park and T. Kouh, Combined effect of mass and stiffness on the dynamics of a double-layered microcantilever, *Appl. Phys. Express*, 2021, **14**, 075004.
35 A. F. Payam and M. Fathipour, Study of the tip mass and interaction force effects on the frequency response and mode shapes of the AFM cantilever, *Int. J. Adv. Manuf. Tech.*, 2013, **65**, 957–966.
36 V. Orsi Gordo, *et al.*, Revealing the nature of lowerature photoluminescence peaks by laser treatment in van der Waals epitaxially grown WS2 monolayers, *Nanoscale*, 2018, **10**, 4807–4815.
37 X. Li and H. Zhu, Two-dimensional MoS2: Properties, preparation, and applications, *J Materiomics*, 2015, **1**, 33–44.
38 P. Yuan, C. Li, S. Xu, J. Liu and X. Wang, Interfacial thermal conductance between few to tens of layered-MoS2 and c-Si: Effect of MoS2 thickness, *Acta Mater.*, 2017, **122**, 152–165.
39 M. Ye, D. Winslow, D. Zhang, R. Pandey and Y. K. Yap, Recent advancement on the optical properties of two-dimensional molybdenum disulfide (MoS2) thin films, *Photonics*, 2015, **2**, 288–307.
40 A. Castellanos-Gomez, M. Poot, G. A. Steele, H. S. J. van der Zant, N. Agraït and G. Rubio-Bollinger, Elastic Properties of Freely Suspended MoS2 Nanosheets, *Adv. Mater.*, 2012, **24**, 772–775.
41 C. Cafolla, K. Voïtchovsky and A. F. Payam, Simultaneous quantification of Young's modulus and dispersion forces with nanoscale spatial resolution, *Nanotechnology*, 2023, **34**, 505714.
42 J. Chang, K. B. Toga, J. D. Paulsen, N. Menon and T. P. Russell, Thickness Dependence of the Young's Modulus of Polymer Thin Films, *Macromolecules*, 2018, **51**, 6764–6770.
43 J. E. Sader, *Frequency Response of Cantilever Beams Immersed in Viscous Fluids with Applications to the Atomic Force Microscope*, 1998.
44 C. Cafolla, A. F. Payam and K. Voïtchovsky, A non-destructive method to calibrate the torsional spring constant of atomic force microscope cantilevers in viscous environments, *J. Appl. Phys.*, 2018, **124**, 154502.
45 B. Łabędź, A. Wańczyk and Z. Rajfur, Precise mass determination of single cell with cantilever-based microbiosensor system, *PLoS One*, 2017, **12**, 1–14.
46 I. Incaviglia, *et al.*, Tailoring the Sensitivity of Microcantilevers To Monitor the Mass of Single Adherent Living Cells, *Nano Lett.*, 2023, **23**, 588–596.
47 Z. W. Huang, *et al.*, Terahertz analysis of $CH_3NH3PbI3$ perovskites associated with graphene and silver nanowire electrodes, *ACS Appl. Mater. Interfaces*, 2021, **13**, 9224–9231.
48 O. Hod, Graphite and hexagonal boron-nitride have the same interlayer distance, Why?, *J. Chem. Theory Comput.*, 2012, **8**, 1360–1369.
49 J. Xu, J. Zhang, W. Zhang and C.-S. Lee, Advanced Energy Materials - 2017 - Xu - Interlayer Nanoarchitectonics of Two–Dimensional Transition–Metal Dichalcogenides.pdf, *Adv. Energy Mater.*, 2017, **7**, 1700571.
50 H. I. Rasool, C. Ophus, W. S. Klug, A. Zettl and J. K. Gimzewski, Measurement of the intrinsic strength of crystalline and polycrystalline graphene, *Nat. Commun.*, 2013, **4**, 2811.
51 L. Torrisi, M. Cutroneo, A. Torrisi and L. Silipigni, Measurements on Five Characterizing Properties of Graphene Oxide and Reduced Graphene Oxide Foils, *Phys. Status Solidi A*, 2022, **219**, 1–9.
52 W. L. Du Frane, O. Cervantes, G. F. Ellsworth and J. D. Kuntz, Consolidation of cubic and hexagonal boron nitride composites, *Diamond Relat. Mater.*, 2016, **62**, 30–41.
53 . The Materials Project. https://legacy.materialsproject.org/.
54 M. L. Pereira Júnior, *et al.*, On the elastic properties and fracture patterns of MoX2 (X = S, Se, Te) membranes: A reactive molecular dynamics study, *Condens. Matter*, 2020, **5**, 1–11.

55 A. Falin, *et al.*, Mechanical Properties of Atomically Thin Tungsten Dichalcogenides: WS2, WSe2, and WTe2, *ACS Nano*, 2021, **15**, 2600–2610.
56 Y. Jiang, *et al.*, Advances in TiS_2 for energy storage, electronic devices, and catalysis: A review, *Prog. Nat. Sci.:Mater. Int.*, 2023, **33**, 133–150.
57 D. G. Papageorgiou, I. A. Kinloch and R. J. Young, Mechanical properties of graphene and graphene-based nanocomposites, *Prog. Mater. Sci.*, 2017, **90**, 75–127.
58 A. Falin, *et al.*, Mechanical properties of atomically thin boron nitride and the role of interlayer interactions, *Nat. Commun.*, 2017, **8**, 1–9.